Journal of Power Sources 438 (2019) 227015

Contents lists available at ScienceDirect

Journal of Power Sources

journal homepage: www.elsevier.com/locate/jpowsour

Fast charging optimization for lithium-ion batteries based on dynamic programming algorithm and electrochemical-thermal-capacity fade coupled model

Meng Xu [a], Rui Wang [b], Peng Zhao [a], Xia Wang [a,*]

[a] Department of Mechanical Engineering, Oakland University, Rochester, MI, 48309, USA
[b] Ford Motor Company, Dearborn, MI, USA

HIGHLIGHTS

- An electrochemical-thermal-capacity fade coupled battery model is developed.
- A multi-stage fast charging protocol is proposed by dynamic programming with model.
- Battery can be fast charged with low capacity fade.
- Battery can be fast charged with a reasonable low temperature rise.

ARTICLE INFO

Keywords:
Fast charging optimization
Lithium ion batteries
Dynamic programming
Electrochemical-thermal-capacity fade model
Cycle life
Heat generation

ABSTRACT

Enabling fast charging of lithium-ion batteries may accelerate the commercial application of electric vehicles (EVs). The fast charging, however, could lead to capacity fade, lithium plating, and thermal runaway. This paper develops an optimal multi-stage charging protocol for lithium-ion batteries to minimize capacity fade due to the solid-electrolyte interphase (SEI) increase, to maximize the SEI potential to decrease the lithium plating, and to reduce the temperature rise to avoid a thermal runaway situation. An electrochemical-thermal-capacity fade coupled model is developed to monitor the battery internal state. The dynamic programming (DP) optimization algorithm is employed to search for the suboptimal charging current profiles. The optimization results illustrate that the optimized charging current profile varies with the state of charge (SOC) and the cycle number. As compared to the constant current charging protocol, each optimized charging strategy can reduce the capacity fade ratio by 4.6%, increase the SEI potential by 57%, and reduce the temperature rise by 16.3% for over 3300 charging-discharging cycles, respectively.

1. Introduction

Fast charging uses battery charging technology that charges the battery faster by increasing the charging power. It is in big demand with electric vehicles (EVs) because charging an EV will always take much longer than refueling a gasoline-powered vehicle and is a possible solution to make up for the EV's limited range [1]. The increased charging power, however, can reduce the battery cycle life due to capacity fade, result in potentially dangerous lithium-plating on the negative electrode, and increase the heat generation [2,3]. The charging protocol with an adaptive charging current profile varying with SOC and/or the cycle life has gained increasing attention [4–11]. Since the internal state of lithium ion batteries such as the internal resistance and the capacity fade varies with SOC and the cycle number, an adaptive charging current profile can help shorten the charging time, increase the energy efficiency, reduce the capacity fade, avoid the lithium-plating, and keep the temperature under control [3,12,13]. The conventional constant current constant voltage (CCCV) charging protocol, however, does not have an adaptive charging current profile because the battery is charged under constant current (CC) until the battery is nearly full [14].

Various charging protocol optimization approaches were proposed to increase charging speed, improve charging energy efficiency, restrain capacity fade, and reduce temperature rise. Vo et al. [4] used one of the Design of Experiment (DOE) methods - Taguchi method to search an

* Corresponding author.
E-mail address: wang@oakland.edu (X. Wang).

https://doi.org/10.1016/j.jpowsour.2019.227015
Received 14 April 2019; Received in revised form 23 June 2019; Accepted 13 August 2019
Available online 20 August 2019
0378-7753/© 2019 Elsevier B.V. All rights reserved.

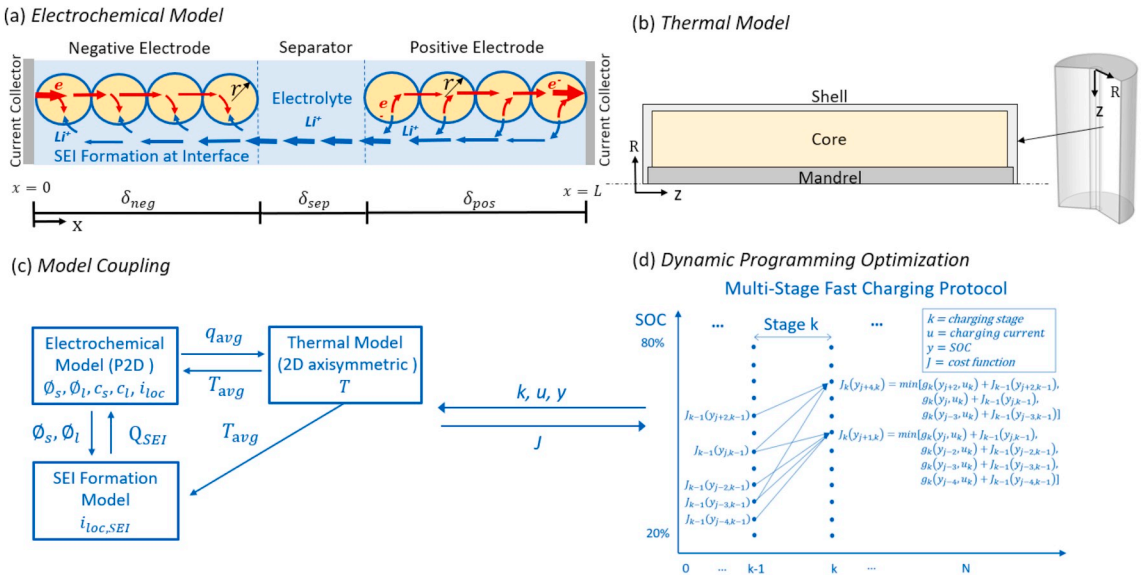

Fig. 1. Schematic of Li-ion cell electrochemical-thermal-capacity fade model coupling and the dynamic programming algorithm for fast charging optimization.

optimal charging current profile of a multi-step constant current (MSCC) protocol, providing shorter charging time, lower temperature rise, and higher energy efficiency than the conventional CCCV charging protocol. Guo et al. [5] proposed an optimal charging protocol using a varying current profile based on an equivalent circuit model and genetic algorithm (GA) technique to improve charging efficiency and cycle life. The proposed current profile varies with the SOC and the cycle number. Zhang et al. [6] utilized the equivalent circuit model and the dynamic programming (DP) optimization algorithm to find an optimal charging protocol under a certain balance between the charging loss and charging time. Hu et al. [7] developed a dual-objective optimal charging strategy using a varying current profile based on an equivalent circuit model and the pseudo-spectral technique to optimally trade off charging time and charging energy loss. Liu et al. [8] developed physics-based single particle model (SPM) and pseudo-spectral method for optimizing charging current profile and online battery control. Side reactions were considered in this work to help avoid cell degradation. In addition, some empirical charging protocols such as constant voltage (CV) [9], linear current decay (LCD) [10], variant current decay (VCD) [9], and CV-CC-CV [11], were proposed for charging optimization.

Those charging protocol optimization methods can be mainly categorized as experiment-based methods [4,9,11] and battery model-based methods combined with certain optimization techniques [5–8] such as genetic algorithm (GA), dynamic programming (DP) algorithm, and pseudo-spectral technique. Since the experiment-based methods are time consuming, the battery model-based optimization methods using the equivalent circuit models [5–7] and the physics-based electrochemical models [8,15] are commonly adopted in the literature. The empirical-based equivalent circuit model requires lower computational cost than the physics-based electrochemical model and is suitable for online battery state estimation and charging optimization [5]. The physics-based model can capture battery internal state such as electrode polarization and capacity fade due to side reactions [8,12,15].

Very few of aformentioned studies considered capacity fade mechanism with charging-discharging cycling while optimizing the charging protocols. In this work, an electrochemical model-based fast charging protocol optimization for a lithium battery cell will be developed to minimize capacity fade due to the SEI increase and the lithium plating with charging-discharging cycles. An electrochemical–thermal–capacity fade coupled model will be developed to monitor battery internal dynamic behaviors such as the SEI increase and polarization potential evolution with charging-discharging cycles. A multistage charging protocol will be utilized with varying charging current levels for each charging stage. The dynamic programming (DP) optimization technique will be used for searching a suboptimal charging protocol for different charging-discharging cycles. Section 2 describes the development of the electrochemical-thermal-capacity fade model, as well as model validation. Section 3 presents the dynamic programming optimization algorithm. Section 4 discusses the charging protocol optimization with various cost functions and constraints and the optimized charging current profile as a function of the SOC and cycle numbers.

2. Electrochemical – thermal – capacity fade model

In this study, a pseudo 2-D (P2D) electrochemical-thermal-capacity fade coupled model will be developed for fast charging protocol optimization to minimize capacity fade due to the SEI increase and the lithium plating in the negative electrode with charging-discharging cycling.

Fig. 1 shows the computational domain for a commercial 26650 $LiFePO_4$ -graphite (LFP) battery cell. The computational model includes **(a)** a P2D electrochemical model for the unit cell **(b)** a 2D thermal model with an axisymmetric geometry for the cell. Since a 1D model in through-plane direction (x) is coupled with a 1D model in radial direction (r), this model is treated as a P2D model.

There are three main components of the unit cell: a Li_yC_6 negative electrode, a separator, and a Li_xFePO_4 positive electrode, where y and x subscripts denote the stoichiometry coefficients of the negative and positive electrodes. This model considers: 1) the charge conservation in the through-plane direction (x); 2) the Li mass conservation in the through-plane direction (x) in the electrolyte phase and in the radius direction (r) of the active particle in the solid phase; 3) the electrochemical kinetics described by Bulter-Volmer equation. The energy conservation is applied to the thermal model. The heat generation rate term, q_{avg}, is the average heat source generated from the local region of the electrochemical cell. The total heat generation rate consists of reversible heat due to entropy change, the irreversible heat due to local overpotential, and the electrical and ionic ohmic heat. The governing equations of the electrochemical-thermal-capacity fade model, model parameters, and model validation are presented in the appendix section.

The degradation of a Li-ion battery cell can be caused by calendar aging which is independent of charge-discharge cycling and cycling aging including the SEI increase and Li plating. During fast charging process, the cycling aging can cause sever capacity fade. The SEI

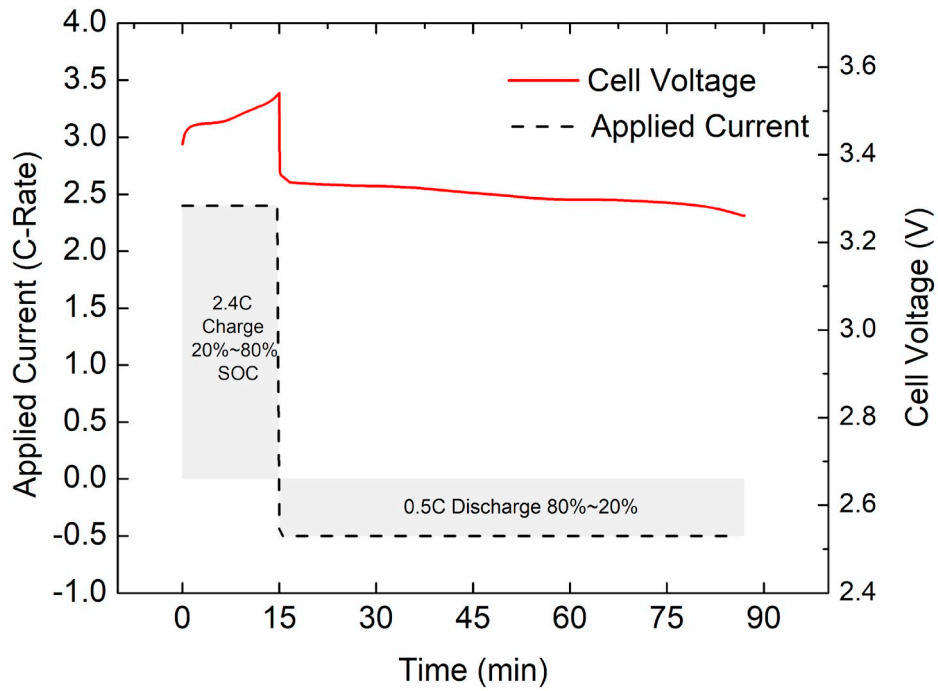

(a)

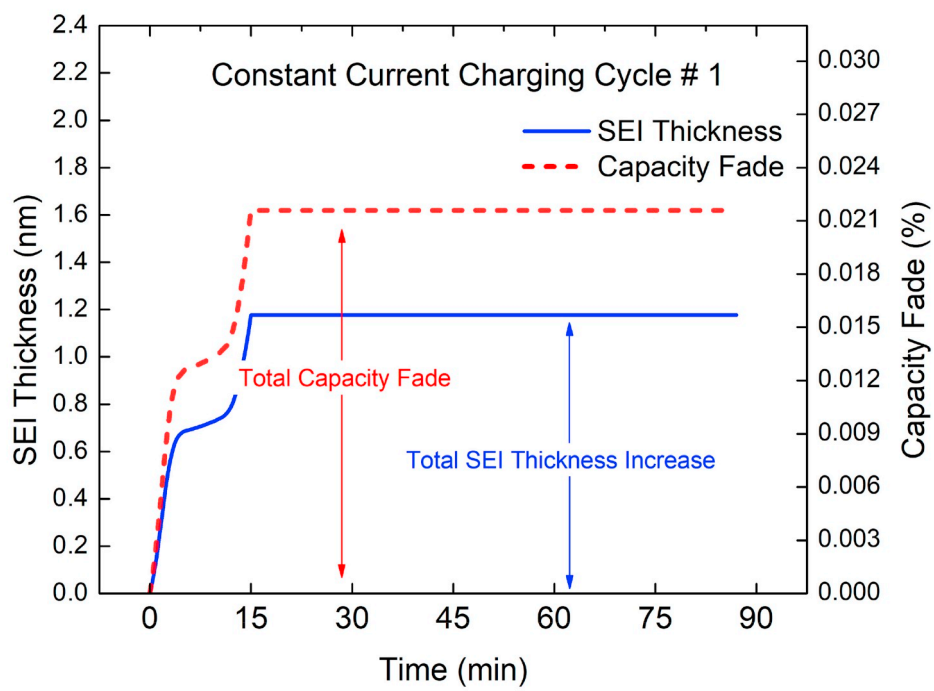

(b)

Fig. 2. (a) Cycling protocol for 2.4 C constant current charge and 0.5 C discharge. (b) SEI thickness evolution and the corresponding capacity fade.

increase contributes more to the capacity fade than Li plating under normal and high temperature, and the Li plating contributes more under low temperatures. This work focuses on the impact of fast-charging on capacity fade at normal temperatures. The capacity fade with charge-discharge cycling is assumed to be contributed by the SEI increase during the charging process. Besides the lithium intercalation reaction on the negative electrode during charging process, a parasitic lithium/solvent (S) reduction reaction is assumed to occur at the interface of the carbon active material [14]. The production of P_{SEI} results in the SEI layer growth and the loss of cyclable lithium in the battery:

$$S + 2Li^{+} + 2e^{-} \rightarrow P_{SEI} \tag{1}$$

The dependent variables in the electrochemical-thermal-capacity fade coupled model include the electrical potential in the solid phase, $\varnothing_s(x,t)$, the ionic potential in the electrolyte phase, $\varnothing_l(x,t)$, the Li concentration in the solid phase, $c_s(x,r,t)$, in the electrolyte phase, $c_l(x,t)$, and in the SEI, $c_{SEI}(x,t)$, the local current density for Li intercalation/deintercalation, $j_{loc}(x,t)$, the local current density for SEI formation, $j_{loc,SEI}(x,t)$, and temperature T.

Fig. 1 (c) shows the electrochemical model and the thermal model

are coupled by the average temperature T_{avg} solved by the thermal model and the average heat generation rate q_{avg} solved by the electrochemical model. The electrochemical model and the SEI formation model are coupled by potentials and the average accumulated charge in the SEI. The coupled electrochemical-thermal-capacity fade model presented in this paper is solved using COMSOL Multiphysics 5.3.

3. Dynamic programming for multi-stage charging protocol optimization

3.1. Dynamic programming

In this paper, Dynamic Programming (DP) technique is applied to the proposed electrochemical-thermal-capacity fade model for fast charging strategy optimization. DP is a mathematical technique for solving a discrete multistage decision problem, in which decisions affecting future stages must be made at a deterministic discrete-finite-state for each stage [16]. The state for each stage is determined by the state of previous stage and the control variable, which can be express as

$$y_{k+1} = f(y_k, u_k) \tag{2}$$

where y_k andu_k represent the state vector and the control vector at kth stage, respectively. The objective of the dynamic programming algorithm is to determine a sequence of control variables, $u_1, u_2, \ldots, u_n$, for a N-stage system by minimizing (maximizing) a cost function J subject to certain constraints, resulting in global optimality. The cost function is in the form of

$$J_k(y_k) = \min_{u_k}[g_k(y_k, u_k) + J_{k-1}(y_{k-1})] \qquad k = 1,\ 2,\ \ldots,\ N,\quad J_0(y_0) = 0 \tag{3}$$

where g_k denotes the cost function of each single stage, and the overall cost function J_k equals to the summation of g_k*and* cost functions of previous stages J_{k-1}. Eq. (3) shows that the overall cost function is evaluated at each stage with corresponding state. It should be noted that when evaluating the cost J_k at different state of y_k, the overall cost function for previous stages J_{k-1} at the state y_{k-1} has already been evaluated and stored. Instead of recomputing $J_{k-1}(y_{k-1})$, one simply looks up the previously computed solution and calculate the single stage cost functions $g_k(y_k, u_k)$, thereby saving computation cost.

3.2. Multi-stage charging protocol optimization

DP is suitable for multi-stage battery charging current level optimization because it can solve a discrete multistage decision problem and guarantee a suboptimal charging current profile. As shown in Fig. 1 (d), k in the abscissa denotes the charging stage, and y in the ordinate represents the SOC. The charging current for each stage is presented by u, which is the control variable. J denotes a cost function for charging optimization such as the SEI thickness and temperature rise. At a certain charging stage k-1, and the corresponding SOC level y_{k-1}, the DP applies various charging current levels $i_{app,k-1}$to the developed battery model as control variables. The model returns the output variables to the DP for computing the cost function $J_k(y_k)$, where the charging stage and SOC are updated (Eq. (4)) because the battery cell is charged to a higher SOC level at the beginning of the stage k.

$$SOC_k = f\left(SOC_{k-1}, i_{app,k-1}\right) \tag{4}$$

The optimization goal is to minimize the cell capacity fade ratio ε_{cf} due to the SEI increase, to maximize the SEI overpotential η_{SEI} to avoid lithium plating, and to minimize the temperature rise to prevent thermal runaway by finding the corresponding charging current profile $i_{app}(k)$ for each charging stage. The cost functions are listed as follows:

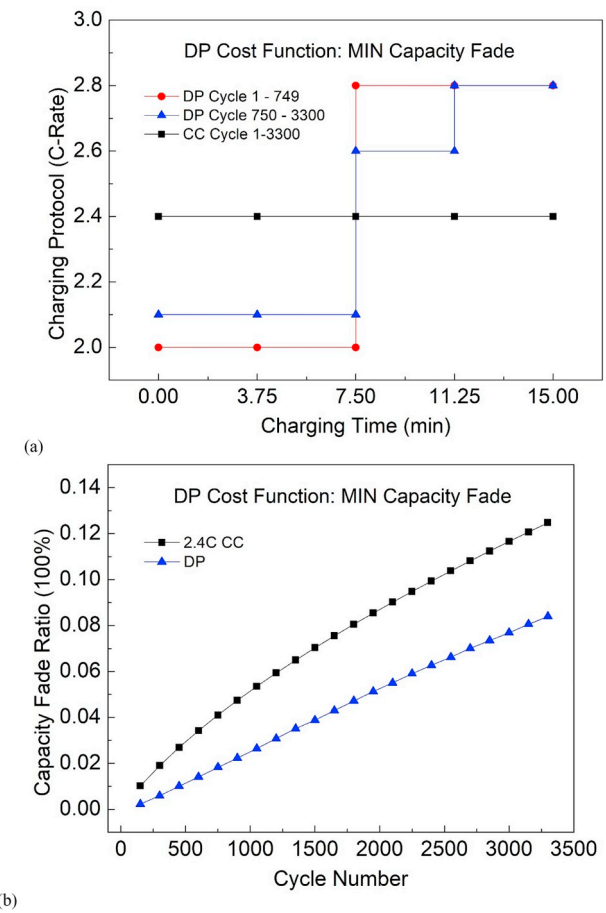

Fig. 3. (a) Optimized charging protocols over 3300 cycles based on dynamic programming algorithm with the minimum capacity fade cost function. (b) Comparison of the capacity fade ratio evolution for the optimized charging protocols and the constant current charging protocol.

$$J_k(SOC_k) = \begin{cases} \min\limits_{u_k}\left[\varepsilon_{cf,k}\left(SOC_k, i_{app,k}\right) + J_{k-1}(SOC_{k-1})\right] \\ \max\limits_{u_k}\left[\eta_{SEI,k}\ \left(SOC_k, i_{app,k}\right) + J_{k-1}(SOC_{k-1})\right] \\ \min\limits_{u_k}\left[T_k\left(SOC_k, i_{app,k}\right) + J_{k-1}(SOC_{k-1})\right] \end{cases} \tag{5}$$

subject to

$$V_k \le V_{max}$$
$$T_k \le T_{max}$$

where V_{max} is the maximum charging cut-off cell voltage, and T_{max} is the maximum allowable operating temperature.

4. Results and discussion

In this study, the charging protocol optimization is conducted for every 150 charging-discharging cycles. The charging current profile is determined by the dynamic programming algorithm. Since the optimization focuses on charging process, the discharging current is set to a constant rate of 0.5 C for each cycle. Fig. 2 (a) shows an example of the charging-discharging protocol and the cell voltage profile for the first cycle. The charging current is assumed to be constant charging rate of 2.4 C, and the cell is charged from 20% to 80% SOC in 15 min, followed by a discharging process from 80% to 20% SOC under 0.5 C-rate. Fig. 2 (b) shows that the corresponding SEI thickness and the cell capacity fade ratio increase during the charging process, while the discharge does not contribute to the SEI increase and capacity fade.

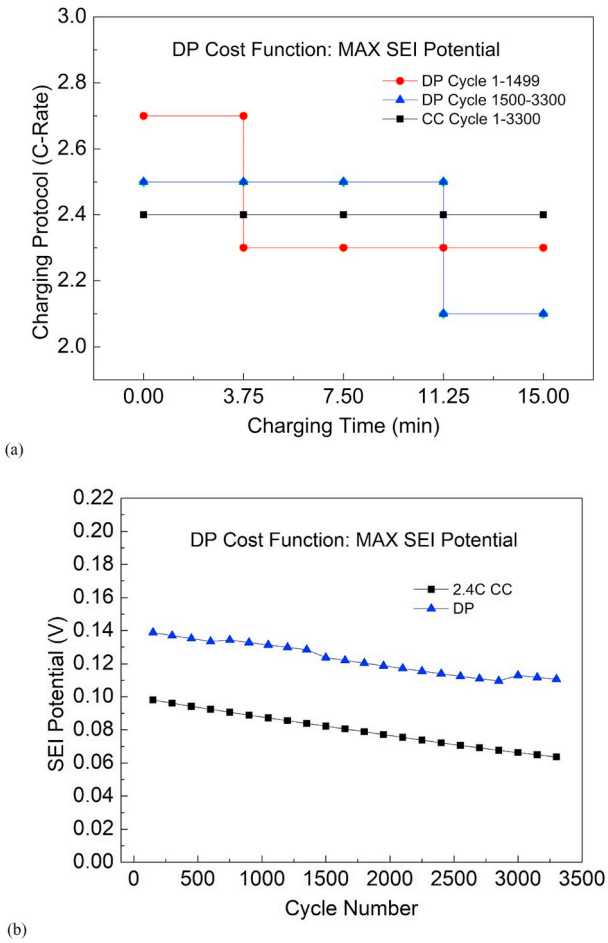

Fig. 4. (a) Optimized charging protocols over 3300 cycles based on dynamic programming algorithm with the maximum SEI potential cost function. (b) Comparison of the SEI potential evolution for the optimized charging protocols and the constant current charging protocol.

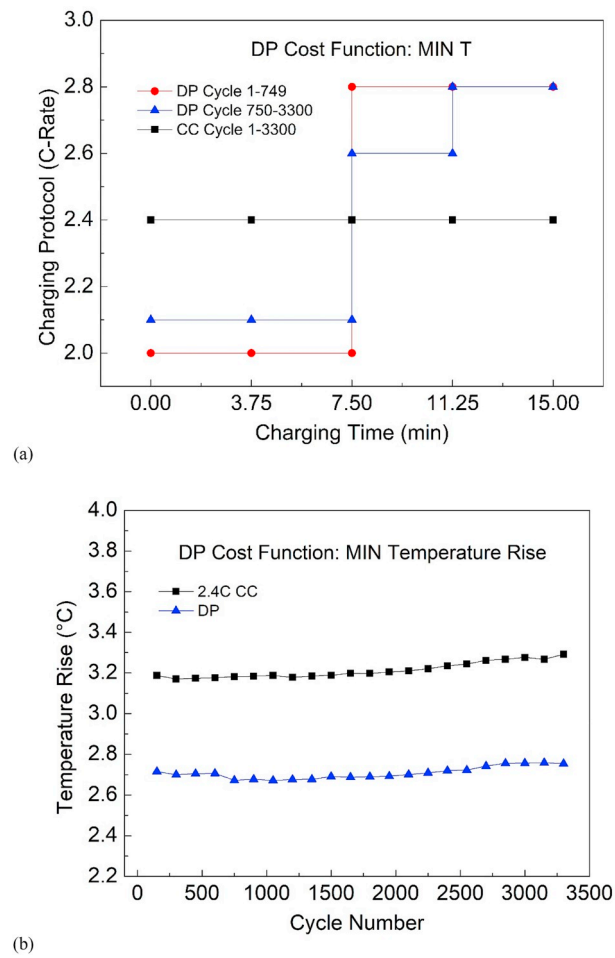

Fig. 5. (a) Optimized charging protocols over 3300 cycles based on dynamic programming algorithm with the minimum temperature rise cost function. (b) Comparison of the temperature rise evolution for the optimized charging protocols and the constant current charging protocol. The initial cell temperature is 25 °C.

Fig. 3 shows that the charging optimization with the cost function of minimizing the capacity fade. A four-stage charging is studied for 3300 charging-discharging cycles. For each cycle, the cycling SOC range is between 20% and 80% with the charging time of 15 min. The CC charging current profile under 2.4 C and the optimized charging current profile using DP are presented in Fig. 3 (a). It is observed that the DP charging current is a function of the charging time and the cycle number. The optimized current level increases with the charging time, and the optimized charging current varies with the cycle number. The optimized charging current level varies with the charging time because the internal state of the cell such as the internal resistance and the graphite expansion coefficient vary with the SOC. The DP ensures that the optimized charging protocol contributes less to the capacity fade than any other charging protocols including the CC protocol. The optimized protocol varies with the cycle number because the internal state of the cell is also affected by the SEI increase. Fig. 3 (b) compares the capacity fade profiles from the CC and DP protocols over 3300 charging-discharging cycles. As compared to the CC protocol, the DP protocol can help reduce the capacity fade ratio by 4.6% after 3300 charging-discharging cycles.

The SEI increase and the lithium plating contribute to the capacity fade in the negative electrode. Although the lithium plating consumes much less cyclable lithium than the SEI, it could lead to the internal short circuit of the cell, resulting in severe safety issue. Note that the SEI potential expressed as the difference between the electrode potential and the electrolyte potential, $\varnothing_S - \varnothing_l$, determines the threshold for lithium plating. During a safe charging process, the electrode potential should be greater than the electrolyte potential, which means the SEI potential is positive. When the charging rate is high and the SOC is high, the SEI potential would be decreased. The Li plating is formed when the SEI potential is negative. To avoid lithium plating during a charging process, the SEI potential should be positive. The optimized fast charging protocol tries to keep the SEI potential away from the lithium plating potential by utilizing a relative high charging current level under the low SOC and a low current level under the high SOC. Fig. 4 (a) shows that the optimized charging protocol with the cost function of maximizing the SEI potential. (Since the SEI potential varies throughout space domain in x-axis of the negative electrode, the SEI potential discussed in Fig. 4 refers to its minimum value, corresponding to the worst case.) The optimized charging current level decreases with the charging time for each cycle. The optimized current profile is switched from the red curve to the blue curve at the cycle # 1500. In Fig. 4 (b), the lowest SEI potential for each charging is monitored under both the DP and the CC protocols. Both curves decrease with the cycle number over 3300 charging-discharging cycles. For the CC charging, the SEI potential decreases from 0.1 V at the first cycle to 0.06 V at the 3300th cycle, which is very close to the lithium plating voltage. To prevent lithium plating, the DP protocol increases the SEI potential by an average ratio of 57% over 3300 cycles.

Heat generation is another consideration for battery fast charging. The high charging current level would generate more heat and further increase the temperature rise, resulting in thermal runaway and higher

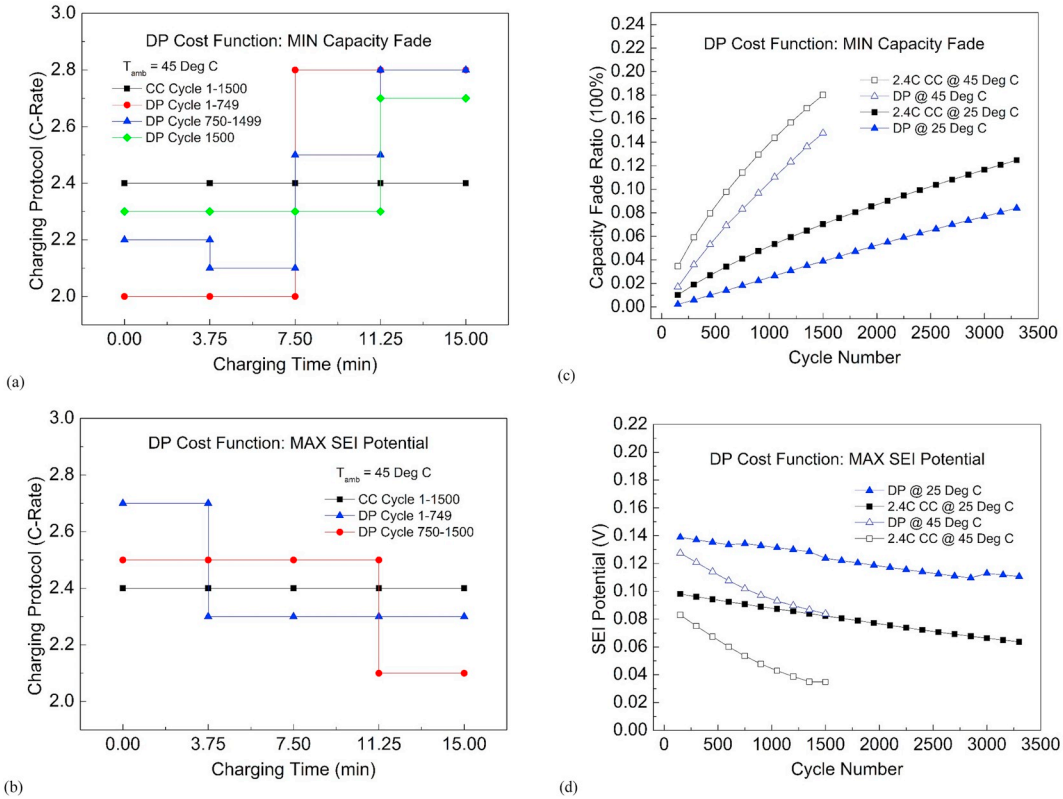

Fig. 6. Optimized charging protocols under 45 °C ambient temperature based on dynamic programming algorithm with the cost function of (a) the minimum temperature rise and (b) the maximum SEI potential. Comparison of (c) the capacity fade ratio evolution and (d) the SEI potential evolution under 25 °C and 45 °C ambient temperature.

design requirement of the battery thermal management system. To reduce the temperature rise, charging optimization is performed using DP with the cost function of minimizing the temperature rise. The initial cell temperature is 25 °C. Fig. 5 (a) shows that the optimized charging current level increases with charging time for each cycle. The optimized profile is switched from the red one to the blue one at cycle # 750. Fig. 5 (b) compares the temperature rise profiles of the DP protocol and the CC protocol, respectively. As compared to the CC protocol, the average temperature rise for the DP protocol over 3300 cycles can be reduced by an average ratio of 16.3% over 3300 charging-discharging cycles.

The DP optimization is performed for the ambient temperature of 25 °C in Figs. 4 and 5. To see the effect of ambient temperature, Fig. 6 (a) and (b) show the optimized charging current profiles under the ambient temperature of 45 °C. The charging patterns are similar to previous results for 25 °C. As shown in Fig. 6 (c) and (d), the temperature rise from 25 °C to 45 °C reduces the SEI potential and thus accelerates the SEI formation rate. The optimized capacity fade at cycle # 1500 under 45 °C has reached 15.1%, which is higher than the capacity fade of 8.5% at cycle # 3300 under 25 °C. The optimized SEI potential of 0.083 V at cycle # 1500 under 45 °C is lower than the potential of 0.104 V at cycle # 3300 under 25 °C. The results indicate that high temperature accelerates the cell degradation, and the DP charging optimization works for different ambient temperatures.

5. Conclusion

This work proposes a fast charging protocol optimization method for lithium ion batteries based on the dynamic programming optimization technique and the physics-based electrochemical-thermal-capacity fade coupled model. The optimization goal is to determine the charging current profile as a function of the SOC (charging stage) and the charging-discharging cycle for a four-stage charging protocol with 15 min charging time and 20%–80% cycling SOC range. The optimization considers various cost functions including reducing the capacity fade due to the SEI increase, increasing the SEI potential to avoid lithium plating, and decreasing the temperature rise to prevent thermal runaway. Comparing with the constant current charging, the proposed multi-stage charge protocol can reduce the capacity fade ratio by 4.6% after 3300 charging-discharging cycles. The SEI potential can be increased by an average ratio of 57% over 3300 charging-discharging cycles. The temperature rise can be reduced by an average ratio of 16.3% over 3300 charging-discharging cycles. In addition, the charging optimization under different ambient temperatures is conducted. The results show that the ambient temperature changing from 25 °C to 45 °C increases capacity fade and decreases the SEI potential (i.e, increases lithium plating). Future research effort will be focusing on finding an optimal fast charging protocol which can create an optimal balance between capacity fade and temperature rise.

Acknowledgements

The authors would like to acknowledge the support of the Provost Graduate Student Research Award at Oakland University and the partial support from the National Science Foundation (grant number: 1542333).

Appendix A

Table A-1 lists the governing equations of the electrochemical-thermal model and corresponding boundary conditions.

Table A-1
Governing equations of the electrochemical-thermal model

Physics	Equations	Boundary conditions
Charge conservation		
(a) Electron in solid	$\frac{\partial}{\partial x}\left(-\sigma_s\frac{\partial \varnothing_s}{\partial x}\right) = -S_a j_{loc}$ (A1)	$\varnothing_s\|_{x=0} = 0;\quad -\sigma_s\frac{\partial \varnothing_s}{\partial x}\|_{x=L} = -i_{app}$
		$\frac{\partial \varnothing_s}{\partial x}\|_{x=\delta_{neg}} = \frac{\partial \varnothing_s}{\partial x}\|_{x=\delta_{neg}+\delta_{sep}} = 0$
(b) Li^+ in electrolyte	$\frac{\partial}{\partial x}\left(-\kappa_{l,eff}\frac{\partial \varnothing_l}{\partial x} - \kappa_{D,eff}\frac{\partial lnc_l}{\partial x}\right) = S_a j_{loc}$ (A2)	$\frac{\partial \varnothing_e}{\partial x}\|_{x=0} = \frac{\partial \varnothing_e}{\partial x}\|_{x=L} = 0$
	Ionic conductivity$\kappa_{l,eff} = \kappa_l \varepsilon_l^{\beta}$ (Bruggeman relation) (A3)	
	Ionic diffusional conductivity $\kappa_{D,eff} = \frac{2RT\kappa_{l,eff}}{F}(t_+ - 1)\left(1 + \frac{\partial lnf_{\pm}}{\partial c_l}\right)$ (A4)	
Mass conservation		
(a) Li in solid	$\frac{\partial c_s}{\partial t} = \frac{D_{s,eff}}{r^2}\frac{\partial}{\partial r}\left(r^2\frac{\partial c_s}{\partial r}\right)$ (A5)	$\frac{\partial c_s}{\partial r}\|_{r=0} = 0;\quad -D_{s,eff}\frac{\partial c_s}{\partial r}\|_{r=R_s} = \frac{j_{loc}}{F}$
(b) Li^+ in electrolyte	$\varepsilon_l\frac{\partial c_l}{\partial t} = \frac{\partial}{\partial x}\left(D_{l,eff}\frac{\partial c_l}{\partial x}\right) + S_a\frac{(1-t_+)}{F}j_{loc}$ (A6)	$\frac{\partial c_l}{\partial x}\|_{x=0} = \frac{\partial c_l}{\partial x}\|_{x=L} = 0$
	Ionic diffusion coefficient$D_{l,eff} = D_l\varepsilon_l^{\beta}$ (Bruggeman relation) (A7)	
Electrochemical kinetics		
(a) Bulter-Volmer equation	$i_{loc} = i_0\left\{exp\left(\frac{\alpha_a F\eta}{RT}\right) - exp\left(\frac{-\alpha_c F\eta}{RT}\right)\right\}$ (A8)	
	Exchange current density$i_0 = Fk_0 c_l^{\alpha_a}(c_{s,max} - c_{s,surf})^{\alpha_a} c_{s,surf}^{\alpha_c}$ (A9)	
	Local electrode overpotential$\eta = \varnothing_s - \varnothing_l - i_{loc}R_{SEI} - U_{eq}$ (A10)	
Energy conservation		
	$\rho C_p\frac{\partial T}{\partial t} = \frac{\partial}{\partial R}\left(\lambda_R\frac{\partial T}{\partial R}\right) + \frac{\partial}{\partial Z}\left(\lambda_Z\frac{\partial T}{\partial Z}\right) + q_{tot}$ (A11)	$-\lambda_{shell}\frac{\partial T}{\partial n}\|_{surface} = h(T - T_{amb})$
	Local heat generation rate$q_{tot} = q_{rev} + q_{irr} + q_{ohm}$ (A12)	
	Reversible entropy heat$q_{rev} = S_a j_{loc} T\frac{\partial U_{eq}}{\partial T}$ (A13)	
	Irreversible reaction heat$q_{irr} = S_a j_{loc}\eta$ (A14)	
	Irreversible ohmic heat$q_{ohm} = \sigma_s(\nabla\varnothing_s)^2 + (\kappa_{l,eff}\nabla\varnothing_l + \kappa_{D,eff}\nabla(lnc_l))\cdot\nabla\varnothing_l$ (A15)	

Table A-2 lists related parameters for the electrochemical model. These parameters were obtained from different sources including published literature, experimental measurement, parameter estimation, and calculation. The particle radii of $LiFePO_4$ for the A123 26650 cell and graphite are available in literature but with different values. A Minimum Mean Square Error (MMSE) [17] estimator is used in this work to estimate the particle radius, the reaction rate constant, and the Bruggeman tortuosity exponent based on the simulation results and experimental data of constant current charging voltage profiles. The SOC of the cell can be calculated based on the stoichiometry in the negative electrode: SOC $= \frac{y - y_{min}}{\Delta y}$, where y is the stoichiometry coefficient, and Δy corresponds to the maximum stoichiometry coefficient utilization range.

Table A-2
Parameters of the electrochemical model

Parameter	Symbol	Unit	Negative Electrode	Separator	Positive Electrode
Electrode thickness	δ	μm	34 [18]	25 [18]	80 [18]
Particle radius	R_s	μm	4[e] (3.58–14.75) [18–22]	–	0.11[e] (0.021–0.169) [18,19,23,24]
Volume fraction of solid phase	ε_s	–	0.549[c]	0.55 [18]	0.354 [23]
Filler volume fraction	ε_f	–	0.0326 [18]	–	0.0535 [18]
Volume fraction of electrolyte (Porosity)	ε_l	–	0.387 [18]	0.45 [18]	0.593 [18,23]
Maximum ***Li*** concentration in solid	$c_{s,max}$	$mol{\cdot}m^{-3}$	30555 [18]	–	22806 [23]
Stoichiometry at 0% cell SOC	y_{min}, x_{max}	–	0.0132 [18]	–	0.74 [18]
Stoichiometry at 100% cell SOC	y_{max}, x_{min}	–	0.811 [18]	–	0.035 [18]
Maximum stoichiometry range	$\Delta y, \Delta x$	–	79.8% [18]	–	70.5% [18]
Initial ***Li*** concentration in electrolyte	$c_{l,0}$	$mol{\cdot}m^{-3}$	1200 [18]		
Li diffusion coefficient in solid	D_s	$m^2{\cdot}s^{-1}$	3.9×10^{-14} [21]	–	1.25×10^{-15} [21]
Li diffusion coefficient in electrolyte	D_l	$m^2{\cdot}s^{-1}$	Eq. (A22) [25]		
Bruggeman tortuosity exponent	β	–	2.5[e]	3.6 [26]	2.1[e]
Electronic conductivity in solid	σ_s	$S{\cdot}m^{-1}$	100 [18]	–	10.8 [20]
Ionic conductivity	κ_l	$S{\cdot}m^{-1}$	Eq. (23) [18]		
Transference number	t_+	–	0.363 [27]		
Reaction rate constant	k_0	$m^{2.5}\,mol^{-0.5}s^{-1}$	2×10^{-11}[e]		1×10^{-12}[e]
Charge-transfer coefficient	α_a, α_c	–	0.5 [23]	–	0.5 [23]
Activation energy for exchange current density	$E_{act}^{i_0}$	$J{\cdot}mol^{-1}$	20000 [18]	–	13000 [18]
Activation energy for solid phase ***Li*** diffusion	$E_{act}^{D_s}$	$J{\cdot}mol^{-1}$	35000 [18]	–	39000 [18]
Activation energy for electrolyte phase ***Li*** diffusion	$E_{act}^{D_l}$	$J{\cdot}mol^{-1}$	26000 [18]		
Activation energy for ionic conductivity of electrolyte	$E_{act}^{\kappa_l}$	$J{\cdot}mol^{-1}$	11000 [18]		
Reference temperature	T_{ref}	K	298.15		
Gas constant	R	$J{\cdot}mol^{-1}K^{-1}$	8.314		
Faraday constant	F	$C{\cdot}mol^{-1}$	96485		
A123 26650 cell nominal capacity	C	Ah	2.3[m]		
Electrode plate area	A	m^2	0.18 [18]		
Applied current density at 1C	$i_{app,\,1C}$	$A{\cdot}m^{-2}$	12.78[c]		

[c] Calculated.
[e] Estimated.
[m] Measured.

Table A-3 provides a summary of the temperature and concentration dependent parameters for active material in the solid phase and the electrolyte phase. The entropy change $\frac{\partial U_{eq,p}}{\partial T}$ and $\frac{\partial U_{eq,n}}{\partial T}$ at different stoichiometry coefficients are obtained from experimental measurement [25,26].

Table A-3
Temperature and concentration dependent variables of the electrochemical model

Physical properties	Equations
Active material in solid	
(1) *Li* diffusion coefficient	$D_{s,i} = D_{s,ref} exp\left(\frac{E_{act}^{D_s}}{R}\left(\frac{1}{T_{ref}} - \frac{1}{T}\right)\right)$ (Arrhenius law) (A16)
(2) Reaction rate constant	$k_{0,i} = k_{0,ref} exp\left(\frac{E_{act}^{k_0}}{R}\left(\frac{1}{T_{ref}} - \frac{1}{T}\right)\right)$ (Arrhenius law) (A17)
(3) Open circuit potentials	$U_{eq,i} = U_{eq,i}(SOC, T_{ref}) + \frac{\partial U_{eq,i}}{\partial T}(T - T_{ref})$ (A18)
Li_xFePO_4	$U_{eq,p}(x) = 2.567462 + 57.69[1 - \tanh(100x + 2.9163927)] + 0.442953tan^{-1}(-65.41928x + 64.89741) + 0.097237tan^{-1}(-160.9058x + 154.590)$ (A19)
Li_yC_6	$U_{eq,n}(y) = 0.7222 + 0.13868y + 0.028952y^{0.5} - 0.017189(1/y) + 0.0019144(1/y^{1.5}) + 0.28082\exp[15(0.06 - y)] - 0.79844\exp[0.44649(y - 0.92)]$ (A20)
Electrolyte	
(1) Li^+ diffusion coefficient	$D_{l,ref}(c_l) = 10^{\left(-8.43 - \frac{54}{T - 229 - 0.005c_l} - 0.0022c_l\right)}$ (A21)
	$D_l = D_{l,ref} exp\left(\frac{E_{act}^{D_l}}{R}\left(\frac{1}{T_{ref}} - \frac{1}{T}\right)\right)$ (Arrhenius law) (A22)
(2) Ionic conductivity	$\kappa_l(c_l) = 8e^{-11}c_l^3 - 4e^{-7}c_l^2 + 0.0006c_l + 0.0151$ (A23)
	$k_l = k_{l,ref} exp\left(\frac{E_{act}^{k_l}}{R}\left(\frac{1}{T_{ref}} - \frac{1}{T}\right)\right)$ (Arrhenius law) (A24)
(3) Thermodynamic factor	$\nu = 0.301 - 0.24\sqrt{10^{-3}c_l} + 0.982[1 - 0.0052(T - 294)\sqrt{10^{-9}c_l^3}]$ (A25)

The physical parameters and geometrical dimensions used in the thermal model are listed in Table A-4.

Table A-4
Physical parameters and geometrical dimensions of the thermal model

Parameter	Symbol	Unit	
Heat capacity	c_p	$J{\cdot}Kg^{-1}K^{-1}$	1100 [18]
Thermal conductivity	λ	$W{\cdot}m^{-1}K^{-1}$	$\lambda_R = 0.35;\ \lambda_z = 36$ [29]
Heat transfer coefficient	h	$W{\cdot}m^{-2}K^{-1}$	5^{e}
Cell lateral surface	A_{cell}	m^2	$6.34 \times 10^{-3\,m}$
Cell volume	$\forall_{cell}$	m^3	$3.42 \times 10^{-5\,m}$
Cell mass	m	Kg	0.07^{m}
Cell density	ρ	$Kg{\cdot}m^{-3}$	2047^{m}
Cell radius	R	mm	12.93^{m}
Cell length	L_{cell}	mm	65.15^{m}

[e] Estimated.
[m] Measured.

The capacity fade mechanism due to the SEI growth is described in Table A-5. Tafel equation is assumed for the kinetics of the solvent reduction reaction (Eq. (26)) [27]. In this equation, $i_{loc,SEI}$ is the local current density on the particle surface of the SEI formation reaction, $i_{loc,1C}$ is the local current density corresponding to 1C rate of the lithium intercalation reaction on the negative electrode, K is a SOC dependent dimensionless graphite expansion factor function, H is a non-dimensional relative expansion factor, J is the dimensionless exchange current density for the SEI formation reaction, α is the transfer coefficient of the electrochemical reduction reaction,$f(1/s)$ is a lumped frequency parameter of the SEI layer properties, η_{SEI} is the overpotential (Eq. (A27)). The local accumulated charge in SEI, q_{SEI}, is proportional to the SEI concentration (Eq. (A28)), where A_v is the electrode specific surface area. The SEI concentration c_{SEI} accumulates according to the reaction rate $i_{loc,SEI}$ (Eq. (A29)), where υ_{SEI} is the stoichiometric coefficient of the SEI. The thickness of the SEI layer δ_{SEI} is calculated from the SEI concentration c_{SEI}, the molar weight M_{SEI} and the density ρ_{SEI}, and the initial SEI layer thickness $\delta_{SEI,0}$ (Eq. (A30)). The resistance of the SEI layer, R_{SEI}, is proportional to the SEI thickness (Eq. (A31)). κ_{SEI} is the electric conductivity of the SEI layer. The cyclable lithium corresponding to the nominal battery capacity decreases with the increase of lithium occupied by the SEI. The relative capacity fade is calculated by (Eq. (A32)), where $\bar{c}_{SEI}$ is the average SEI concentration over the computational domain of the negative electrode. The initial value for ε_{cf} is set to 0 at the beginning of the first cycle.

Table A-5
Governing equations of the capacity fade model

Physics	Equations
Solvent reduction reaction	$j_{loc,SEI} = (1+hk)\dfrac{j_{loc,1C}}{\exp\left(\dfrac{\alpha\eta_{SEI}F}{RT}\right)+\dfrac{q_{SEI}fJ}{j_{loc,1C}}}$ (A26)
SEI potential	$\eta_{SEI} = \varnothing_s - \varnothing_l - U_{eq,SEI}(0.4V)$ (A27)
Local accumulated charge in SEI	$q_{SEI} = \dfrac{Fc_{SEI}}{A_v}$ (A28)
Li concentration increase rate in SEI	$\dfrac{\partial c_{SEI}}{\partial t} = -\dfrac{\upsilon_{SEI}j_{loc,SEI}}{nF}$ (A29)
SEI thickness	$\delta_{SEI} = \dfrac{c_{SEI}M_{SEI}}{A_v\rho_{SEI}} + \delta_{SEI,0}$ (A30)
SEI resistance	$R_{SEI} = \dfrac{\delta_{SEI}}{\kappa_{SEI}}$ (A31)
Capacity fade ratio	$\varepsilon_{cf} = \dfrac{\bar{c}_{SEI}}{c_{s,neg,max}\Delta y}$ (A32)

A 2.3 Ah commercial *LFP* cell (ANR26650 M1-B) from A123 Systems is tested for the model validation. The battery cell was charged from 0% SOC at five different constant current rates (0.7 C, 1 C, 1.6 C, 2 C, 3.2 C) up to 3.65 V limit using the Maccor Battery automation system. The initial temperature of the cell is equal to the ambient room temperature of 25 °C. The average surface temperature of the cell is measured experimentally using three thermocouples evenly distributed over the cell surface. The heat generated from the cell is removed from the cell by natural convection at the cell surface. The heat transfer coefficient is determined by fitting the modeling results to experimental data. Fig. A1 compares modeling results and experimental data. Figure A-1 (a)and (b) shows the measured charging voltage and the surface temperature agree with the model predictions for different rates of charge. The modeling results of the capacity fade with charge-discharge cycling are also compared with some literature data of *LFP* cells under various ambient temperatures and charge-discharge cycling SOC in Fig A-1 (c). The simulation results agree well with the experimental data. This model is used in the paper in conjunction with the dynamic programming technique to optimize the cell charging strategy.

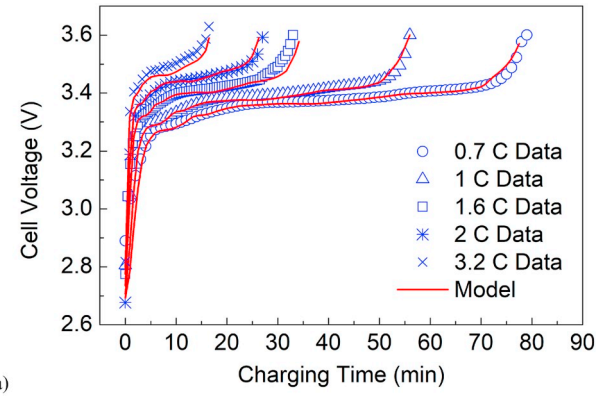

(a)

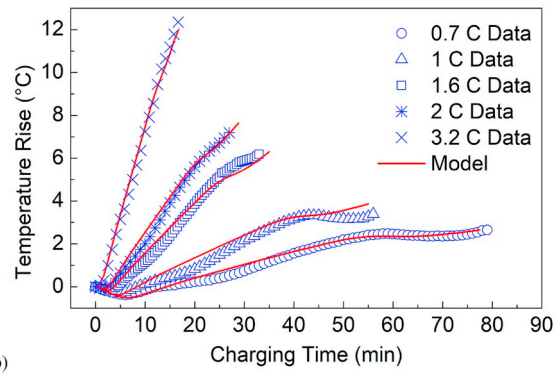

(b)

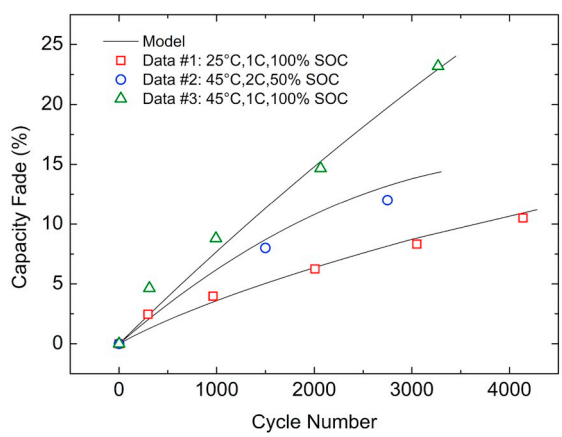

(c)

Fig. A1. Comparison of the modeling results and the experimental data for (a) Charging voltage and (b) surface temperature at various C-rates and ambient temperature of 25 °C. (c) Capacity fade validation using literature data (#1 [30], #2 [28], #3 [30]) for various ambient temperatures and charge-discharge cycling SOC.

Appendix A. Supplementary data

Supplementary data to this article can be found online at https://doi.org/10.1016/j.jpowsour.2019.227015.

Nomenclature

A	electrode plate area (cm^2)
A_{cell}	cell surface area (m^2)
C_{cell}	nominal capacity (Ah)
c_p	heat capacity ($J \cdot Kg^{-1}K^{-1}$)
c_s	concentration of lithium in the active material particles (mol m^{-3})
c_l	electrolyte concentration (mol m^{-3})
D_s	diffusion coefficient of lithium in the active material (m^2 s^{-1})

D_l	diffusion coefficient of electrolyte ($m^2\ s^{-1}$)
E_{act}	activation energy ($J\ mol^{-1}$)
E_{in}	charging energy (Wh)
$f_{\pm}$	average molar activity coefficient
F	Faraday's constant ($C\ mol^{-1}$)
q	heat generation rate ($W\ m^{-3}$)
h	heat transfer coefficient ($W \cdot m^{-2} K^{-1}$)
j_0	exchange current density ($A\ m^{-2}$)
j_{loc}	local charge transfer current density ($A\ m^{-2}$)
k_0	reaction rate constant ($m^{2.5}\ mol^{-0.5} s^{-1}$)
R	gas constant, 8.314 ($J\ mol^{-2} K^{-1}$)
R_0	radius of electrode particles (μm)
S_a	specific surface area (m^{-1})
t_+	transference number of lithium ions
T	temperature (K)
U_{eq}	open circuit potential of the electrode (V)
$\forall_{cell}$	cell volume (m^3)

Greek letters

α_a	anodic transfer coefficient
α_c	cathodic transfer coefficient
β	Bruggeman porosity exponent
λ	thermal conductivity ($W \cdot m^{-1} K^{-1}$)
ε_s	active material volume fraction
ε_l	electrolyte volume fraction or porosity
$\varnothing_s$	solid phase potential (V)
$\varnothing_l$	electrolyte phase potential (V)
σ_s	electronic conductivity of solid matrix ($S\ m^{-1}$)
κ_l	ionic conductivity of electrolyte ($S\ m^{-1}$)
δ	thickness of each battery component (μm)
η	local surface overpotential (V)

Subscripts, superscripts and acronyms

0	initial or equilibrated value
s	solid phase
l	electrolyte phase
cf	capacity fade
eff	effective value
Pos	positive electrode
sep	separator
ref	reference value

References

[1] D. Anseán, M. Dubarry, A. Devie, B.Y. Liaw, V.M. García, J.C. Viera, M. González, Fast charging technique for high power LiFePO4 batteries: a mechanistic analysis of aging, J. Power Sources 321 (2016) 201–209.

[2] Xiao-Guang Yang, Yongjun Leng, Guangsheng Zhang, Shanhai Ge, Chao-Yang Wang, Modeling of lithium plating induced aging of lithium-ion batteries: transition from linear to nonlinear aging, J. Power Sources 360 (2017) 28–40.

[3] Ravi Methekar, Venkatasailanathan Ramadesigan, Richard D. Braatz, Venkat R. Subramanian, Optimum charging profile for lithium-ion batteries to maximize energy storage and utilization, ECS Trans. 25 (35) (2010) 139–146.

[4] T.T. Vo, X. Chen, W. Shen, A. Kapoor, New charging strategy for lithium-ion batteries based on the integration of Taguchi method and state of charge estimation, J. Power Sources 273 (2015) 413–422.

[5] Zhen Guo, Bor Yann Liaw, Xinping Qiu, Lanlan Gao, Changshui Zhang, Optimal charging method for lithium ion batteries using a universal voltage protocol accommodating aging, J. Power Sources 274 (2015) 957–964.

[6] Shuo Zhang, Chengning Zhang, Rui Xiong, Wei Zhou, Study on the optimal charging strategy for lithium-ion batteries used in electric vehicles, Energies 7 (10) (2014) 6783–6797.

[7] Xiaosong Hu, Shengbo Li, Huei Peng, Fengchun Sun, Charging time and loss optimization for LiNMC and LiFePO4 batteries based on equivalent circuit models, J. Power Sources 239 (2013) 449–457.

[8] J. Liu, G. Li, H.K. Fathy, A computationally efficient approach for optimizing lithium-ion battery charging, J. Dyn. Syst. Meas. Control 138 (2) (2016), 021009.

[9] G. Sikha, P. Ramadass, B.S. Haran, R.E. White, B.N. Popov, Comparison of the capacity fade of Sony US 18650 cells charged with different protocols, J. Power Sources 122 (2003) 67–76.

[10] S.K. Chung, A.A. Andriiko, A.P. Mon'ko, S.H. Lee, On charge conditions for Li-ion and other secondary lithium batteries with solid intercalation electrodes, J. Power Sources 79 (1999) 205–211.

[11] P.H.L. Notten, J.H.G. Op het Veld, J.R.G. Van Beek, Boostcharging Li-ion batteries: a challenging new charging concept, J. Power Sources 145 (2005) 89–94.

[12] Meng Xu, Rui Wang, Benjamin Reichman, Xia Wang, Modeling the effect of two-stage fast charging protocol on thermal behavior and charging energy efficiency of lithium-ion batteries, J. Energy Storage 20 (2018) 298–309.

[13] Sourav Pramanik, Sohel Anwar, Electrochemical model based charge optimization for lithium-ion batteries, J. Power Sources 313 (2016) 164–177.

[14] R.C. Cope, Y. Podrazhansky, The art of battery charging, in: Battery Conference on Applications and Advances, 1999, pp. 233–235.

[15] Eric Prada, D. Di Domenico, Y. Creff, J. Bernard, Valérie Sauvant-Moynot, François Huet, A simplified electrochemical and thermal aging model of LiFePO4-graphite li-ion batteries: power and capacity fade simulations, J. Electrochem. Soc. 160 (4) (2013) A616–A628.

[16] Rui Wang, M. Lukic Srdjan, Dynamic programming technique in hybrid electric vehicle optimization, in: 2012 IEEE International Electric Vehicle Conference, IEEE, 2012, pp. 1–8.

[17] J. Remmlinger, M. Buchholz, M. Meiler, P. Bernreuter, K. Dietmayer, State-of-health monitoring of lithium-ion batteries in electric vehicles by on-board internal resistance estimation, J. Power Sources 196 (2011) 5357–5363.

[18] E. Prada, D.D. Domenico, Y. Creff, J. Bernard, Simplified electrochemical and thermal model of LiFePO4-graphite Li-ion batteries for fast charge applications, J. Electrochem. Soc. 159 (2012) A1508–A1519.

[19] C. Hellwig, S. Sörgel, W.G. Bessler, A multi-scale electrochemical and thermal model of a LiFePO4 battery, Ecs Trans. 35 (32) (2011) 215–228.

[20] M. Doyle, J. Newman, A.S. Gozdz, C.N. Schmutz, J.M. Tarascon, Electrochem. Soc. 143 (1996) 1890.

[21] F. Jiang, P. Peng, Y. Sun, Thermal analyses of LiFePO 4/graphite battery discharge processes, J. Power Sources 243 (2013) 181–194.
[22] B. Jin, H.B. Gu, W. Zhang, K.H. Park, G. Sun, Effect of different carbon conductive additives on electrochemical properties of LiFePO4-C/Li batteries, J. Solid State Electrochem. 12 (2008) 1549–1554.
[23] M. Farkhondeh, C. Delacourt, Mathematical modeling of commercial LiFePO4 electrodes based on variable solid-state diffusivity, J. Electrochem. Soc. 159 (2011) A177–A192.
[24] M. Safari, C. Delacourt, Mathematical modeling of lithium iron phosphate electrode: galvanostatic charge/discharge and path dependence, J. Electrochem. Soc. 158 (2) (2011) A63–A73.
[25] R.G. Gerver, J.P. Jeremy, P. Meyers, Three-dimensional modeling of electrochemical performance and heat generation of lithium-ion batteries in tabbed planar configurations, J. Electrochem. Soc. 158 (2011) A835–A843.
[26] K. Jalkanen, T. Aho, K. Vuorilehto, Entropy change effects on the thermal behavior of a LiFePO4/graphite lithium-ion cell at different states of charge, J. Power Sources 243 (2013) 354–360.
[27] S.J. Bazinski, X. Wang, B.P. Sangeorzan, L. Guessous, Measuring and assessing the effective in-plane thermal conductivity of lithium iron phosphate pouch cells, Energy 114 (2016) 1085–1092.
[28] Henrik Ekström, Göran Lindbergh, A model for predicting capacity fade due to SEI formation in a commercial graphite/LiFePO4 cell, J. Electrochem. Soc. 162 (6) (2015) A1003–A1007.
[29] M. Safari, C. Delacourt, Aging of a commercial graphite/LiFePO4 cell, J. Electrochem. Soc. 158 (2011) 1123–1135.
[30] J. Wang, P. Liu, J.H. Garner, E. Sherman, S. Soukiazian, M. Verbrugge, H. Tataria, J. Musser, P. Finamore, Cycle-life model for graphite-LiFePO4 cells, J. Power Sources 196 (2011) 3942–3948.